

CO₂ imaging with saturated planar laser-induced vibrational fluorescence

Brian J. Kirby and Ronald K. Hanson

We present new vibrational (infrared) planar laser-induced fluorescence (PLIF) imaging techniques for CO₂ that use a simple, inexpensive, high-pulse-energy transversely excited atmospheric CO₂ laser to saturate a CO₂ absorption transition at 10.6 μm. Strong excitation by use of a CO₂ laser provides increased signal levels at flame temperatures and simplifies image interpretation. Because rotational energy transfer and intramodal vibrational energy transfer are fast, vibrational distributions can be approximated by use of a simple three-temperature model. Imaging results from a 425 K unsteady transverse CO₂ jet and a laminar coflowing CO/H₂ diffusion flame with temperatures near 1500 K are presented. If needed, temperature-insensitive signal levels can be generated with a two-laser technique. These results illustrate the potential for saturated infrared PLIF in a variety of flows. © 2001 Optical Society of America

OCIS codes: 300.2530, 300.6340, 111.3080, 260.2510.

1. Introduction

Recent studies have investigated infrared (IR) variations of planar laser-induced fluorescence (PLIF) techniques,^{1–3} which involve use of an IR laser source to excite vibrational transitions in IR-active molecules and IR cameras to collect vibrational fluorescence. These studies have included imaging of CO at isothermal, room-temperature conditions,¹ imaging of CO and CO₂ in flames,² and a computational analysis of linear IR PLIF excitation schemes for CO and CO₂.³ Because IR PLIF measurements can generate high signal levels that scale linearly with both laser energy and species concentration, IR PLIF demonstrates advantages over Raman⁴ and multiphoton PLIF^{5–7} techniques to image species with inconvenient or inaccessible electronic spectra. As an example, IR PLIF is unique in that it provides the ability to image nascent CO₂ in combustion systems on a single-shot basis; this can be employed to identify combustion product regions or

to measure mixing between postcombustion gases and ambient air or fuel–air charge. IR PLIF can thus serve as a valuable tool to evaluate combustion system designs.

In this paper we use a simple, inexpensive, high-pulse-energy IR gas laser to generate planar laser-saturated IR fluorescence. As compared with previous CO₂ imaging schemes,^{2,3} which employed tunable optical parametric oscillators to excite transitions in the linear regime, gas laser excitation in the saturated regime generates a larger PLIF signal at combustion temperatures and simplifies image interpretation by minimizing inhomogeneities in fluorescence yield. We present simple theoretical results for IR PLIF signal levels in the saturated regime, evaluate saturation of the absorption transition and its effects on PLIF signal dependence, and demonstrate saturated PLIF imaging of CO₂.

2. Background

In this section we describe how saturated excitation simplifies interpretation of PLIF signals, provide a simple model for the saturated PLIF signal dependence, and support the validity of this model with a detailed rate equation analysis. When we use an integrating detector (e.g., an IR camera) and collection optics with efficiency η_c , the laser-induced fluorescence (LIF) signal S_f is equal to the integration of

When this research was performed, the authors were with the Department of Mechanical Engineering, Stanford University, Stanford, California 94309. B. J. Kirby (bjkirby@sandia.gov) is now with the Microfluidics Department, Sandia National Laboratories, P.O. Box 969, Mail Stop 9951, Livermore, California 94551.

Received 22 January 2001; revised manuscript received 23 July 2001.

0003-6935/01/336136-09\$15.00/0

© 2001 Optical Society of America

the rate of LIF \mathcal{F} over the exposure time τ , multiplied by the collection efficiency:

$$S_f = \int_0^\tau \mathcal{F}(t) dt \eta_c. \quad (1)$$

The rate of LIF from each excited state j is given by the product of the laser-induced change in the state population $\Delta N_j(t)$ and the Einstein A emission rate from that state A_j . Summing over all states, we obtain

$$S_f = \sum_j \int_0^\tau \Delta N_j(t) A_j dt \eta_c. \quad (2)$$

In the linear (weak) excitation limit, the absorption process does not significantly perturb the system, and Eq. (2) can be rearranged to separate the processes of absorption and emission. The number of absorbed photons $N_{p,abs}$ is given by the number of incident photons $N_{p,inc}$ times the absorbed fraction:

$$N_{p,abs} = N_{p,inc} n_{abs} \sigma l, \quad (3)$$

where n_{abs} is the number density of the interrogated species, σ is its absorption cross section, and l is the length of the imaged region. The fluorescence quantum yield ϕ_{lin} is then defined as the number of emitted photons normalized by $N_{p,abs}$:

$$\phi_{lin} = \sum_j \int_0^\tau \frac{\Delta N_j(t)}{N_{p,abs}} A_j dt. \quad (4)$$

ϕ_{lin} is typically inversely proportional to the rate at which vibrational energy is removed from the fluorescing species. With these definitions, the fluorescence equation can be written as

$$S_{f,lin} = N_{p,inc} n_{abs} \sigma l \phi_{lin} \eta_c. \quad (5)$$

The format of Eq. (5) provides insight into the effect of parameters on the fluorescence signal. $N_{p,inc}$ is dictated by laser-pulse energy, η_c by the collection optics and camera, $n_{abs} \sigma l$ by the absorption properties of the interrogated species, and ϕ_{lin} by the magnitudes of excited-state emission rates and the collisional interaction between the interrogated species and its environment. In particular, ϕ_{lin} embodies the effects of the energy-transfer processes with the bath gas. Successful linear PLIF techniques require that ϕ_{lin} be roughly independent of the bath gas species makeup so that S_f can be directly related to n_{abs} by Eq. (5). This is easily achieved for some species (e.g., CO³). However, for CO₂, the rate at which vibrational energy is removed from the emitting states is orders of magnitude higher for collisions with H₂O than it is for collisions with other species; thus ϕ_{lin} varies significantly as a function of the H₂O mole fraction in the bath gas. This makes interpretation of CO₂ concentration based on the linear IR PLIF signal difficult in combustion environments.

We have applied saturated excitation as a means of

avoiding the complexity of signal interpretation for PLIF of CO₂ in the linear regime. When the transition is saturated with a high-pulse-energy laser, the upper- and lower-level populations are driven to be equal (when we neglect differences in state degeneracies) and are thus roughly constant throughout the pulse. For saturated fluorescence, it is therefore more convenient to use the fluorescence yield ψ_{sat} , which is defined as the number of emitted photons normalized by the number of absorbing molecules $n_{abs}V$ in the irradiated volume:

$$\psi_{sat} = \sum_j \int_0^\tau \frac{\Delta N_j(t)}{n_{abs}V} A_j dt. \quad (6)$$

Note that ψ_{sat} is an overall fluorescence yield, defined as fluorescence photons per molecule of the interrogated species, in contrast to ϕ_{lin} , which is a fluorescence quantum yield, defined as fluorescence photons per absorbed photon. With this definition, the fluorescence equation takes a simple form:

$$S_{f,sat} = \psi_{sat} n_{abs} V \eta_c. \quad (7)$$

Because for isobaric flows we are most often interested in mole fractions rather than concentration, we can use the definition of the mole fraction ($\chi_{abs} = n_{abs}/n$) and the ideal gas law ($P = nk_B T$) to rearrange Eq. (7) to show the fluorescence signal as a function of the mole fraction:

$$S_{f,sat} = \frac{\psi_{sat}}{T} \chi_{abs} \frac{PV}{k_B} \eta_c. \quad (8)$$

Because we can easily calibrate V and η_c experimentally, for isobaric flows ψ_{sat}/T is the only parameter that need be calculated to quantify the CO₂ mole fraction from the PLIF signal. In Subsections 2.A and 2.C we show that ψ_{sat}/T can show much less sensitivity to bath gas constituents than ϕ_{lin} and less sensitivity to temperature than σ .

A transversely excited atmospheric (TEA) CO₂ laser is used in this study as an IR PLIF source to saturate the $P(20)$ transition of the $00^0_1 \leftarrow 10^0_1$ band of CO₂ for IR PLIF imaging (see Ref. 8 for CO₂ vibrational state notation). The energy-transfer processes relevant to 10.6- μ m excitation are shown in Fig. 1. Although a full description of the state-to-state energy transfer including rotational energy transfer (RET) and vibrational energy transfer (VET) can be used for precise calculations of ψ_{sat} , an investigation of the characteristic rates of energy transfer for this system shows that this system is approximately described by a simple three-temperature model. The structure of the CO₂ vibrational manifold and characteristic rates of VET processes are discussed in the Subsections 2.A and 2.B and motivate Subsection 2.C on the three-temperature model that is used to explain the dependence of the IR PLIF signal with temperature.

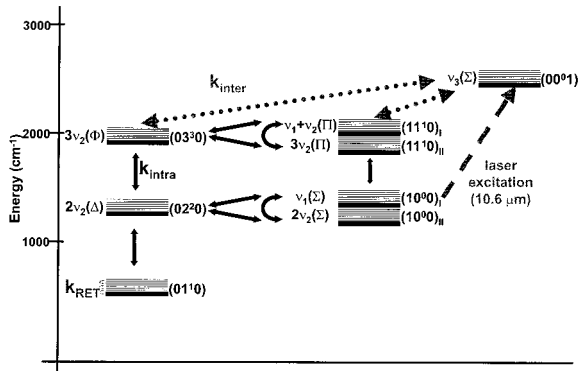


Fig. 1. Vibrational manifold showing energy-transfer processes for CO₂ during and after laser excitation at 10.6 μm on the P(20) line of the 00⁰₁ ← 10⁰₁ transition. Notation to the right of each state follows the convention of Ref. 8 and notation to the left of each state follows the convention of Ref. 9. k_{inter} corresponds to the characteristic rate of intermodal energy-transfer processes that equilibrate ν_3 with the other modes; k_{intra} corresponds to the characteristic rate of intramodal energy-transfer processes that equilibrate ν_1 and ν_2 alone. k_{RET} is the rate at which the lower and upper rotational states of the laser transition equilibrate with the rotational bath.

A. CO₂ Vibrational Manifold

The vibrations of CO₂ are coupled and anharmonic, exhibit Fermi resonance (between ν_1 and $2\nu_2$), and are in some cases degenerate (ν_2). Thus the vibrational wave functions are not accurately described by use of the harmonic-oscillator wave functions, and the vibrational level notation must distinguish between Fermi-resonant levels and levels with different angular momentum.⁸ Despite their spectroscopic importance, however, these details can be ignored for calculations of energy transfer among the lower vibrational levels because they do not significantly affect state populations or transfer rates. Detailed calculations in Subsection 2.C confirm that a harmonic-oscillator analysis is accurate for calculation of fluorescence yield.

For the purposes of evaluating laser-perturbed state distributions and the fluorescence yield ψ_{sat} , we assume that the vibrational energy levels of CO₂ are described by four independent and harmonic vibrational modes (nondegenerate ν_1 and ν_3 , doubly degenerate ν_2). For each vibrational mode, we define a characteristic temperature Θ such that the product of the Boltzmann constant k_B and the characteristic temperature are equal to the vibrational energy spacing.¹⁰ For CO₂, $\Theta_1 = 2000$ K, $\Theta_2 = 960$ K, and $\Theta_3 = 3380$ K. Because each mode is treated as harmonic, the quantum number of each vibrational level is an approximate measure of how many quanta of vibrational energy the vibrational level possesses at each vibrational frequency. Furthermore, because each mode is treated as being independent, it can be considered to have its own energy distribution that is unaffected by the distribution of the energy of other modes. For example, the distribution of ν_3 quanta among the CO₂ molecules is treated as independent

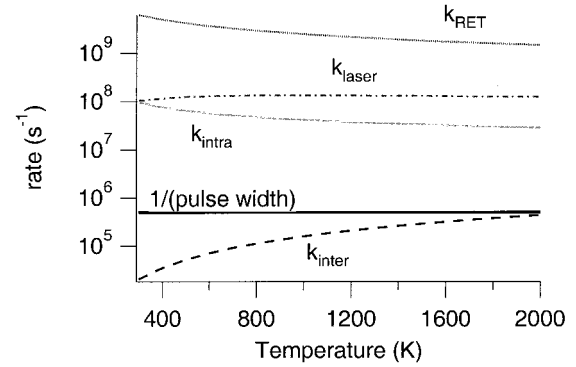


Fig. 2. Important energy-transfer rates as a function of temperature for CO₂. We calculated k_{laser} assuming $dE/dt = 2.5 \times 10^6$ J/s and sheet dimensions of 500 μm × 4 cm. For the line-shape convolution integral, the laser was modeled as a 300-MHz Gaussian.

of the distribution of ν_1 or ν_2 quanta and, if Boltzmann, can be described with a vibrational temperature T_3 .

B. Characteristic Rates

The three-temperature model discussed in Subsection 2.C is motivated by the relative magnitudes of the characteristic rates of (1) laser pumping, (2) equilibration of the rotational state distribution with the translational temperature, (3) intramodal equilibration of individual modes, (4) equilibration of ν_1 with ν_2 , and (5) intermodal equilibration between the ν_3 mode and the other modes. These characteristic rates are plotted in Fig. 2 as a function of temperature for CO₂.

The characteristic rate of laser pumping is

$$k_{\text{laser}} = \frac{dN}{dt} \frac{\sigma}{A_L}, \quad (9)$$

where dN/dt is the instantaneous rate of incident photons and A_L is the cross-sectional area of an idealized top-hat sheet waist. k_{laser} is the characteristic rate at which CO₂ molecules in the 10⁰₁ level are pumped to the 00⁰₁ level.

k_{RET} , the characteristic rate of RET, is defined as the rate of equilibration of the lower state of the laser transition with the bath of rotational states in the lower vibrational level:

$$k_{\text{RET}} \equiv \sum_{\substack{j=1 \\ j \neq i}}^{\infty} k_{i \rightarrow j} = 2\pi c \nu_{c_i}. \quad (10)$$

Here the summed RET rate is assumed proportional to the HWHM collisional broadening coefficient of the pumped line ν_{c_i} (cm⁻¹) times the speed of light c

(cm/s). $k_{i \rightarrow j}$ is the rate of transfer between rotational states i and j :



Elastic dephasing and rotation–rotation interactions were ignored in Eq. (10) because elastic dephasing is a negligible contribution to broadening, and rotation–rotation considerations are not required to satisfactorily describe RET in CO_2 .^{11–22}

Characteristic rates of intermodal and intramodal energy transfer are defined with prototypical energy-transfer reactions for CO_2 . Because ν_1 and ν_2 behave to a good approximation as a single mode, we group near-resonant energy transfer between ν_1 and ν_2 with intramodal processes for purposes of this discussion. The transfer among the $10^0 0_{\text{I}}$, $10^0 0_{\text{II}}$, and $02^2 0$ levels is the most important intramodal process for the 10.6- μm pumping scheme; and the rate of the $\text{CO}_2(02^2 0) + \text{M} \leftrightarrow \text{CO}_2(10^0 0_{\text{I}}) + \text{M}$ reaction is taken as k_{intra} , the rate characteristic of intramodal equilibration for display in Fig. 2. Intermodal equilibration among the ν_3 mode and other modes occurs primarily through $\text{CO}_2(00^0 1) + \text{M} \leftrightarrow \text{CO}_2(11^0 0_{\text{I}}) + \text{M}$ and similar reactions, all of which are much less efficient.^{23,24} This sum of intermodal energy-transfer rates is plotted as k_{inter} in Fig. 2 as representative of intermodal equilibration.

C. Three-Temperature Model

Because of the relative magnitudes of the rates shown in Fig. 2, the most convenient interpretation of the laser-induced state distributions is a three-temperature model that employs the harmonic-oscillator approximation. This model will lead to a relation for the fluorescence yield ψ_{sat} as a function of temperature.

The magnitudes of the rates shown in Fig. 2 imply that the five temperatures (T_{tr} , T_{rot} , T_1 , T_2 , T_3) are all well defined and collapse to three independent temperatures that define the nonequilibrium (laser-perturbed) vibrational distribution. RET is fast, so the rotational distribution in each vibrational level is Boltzmann with a well-defined rotational temperature equal to the translational temperature. Thus, even though the laser pumps only the $j = 20$ state directly, all rotational states in the $10^0 0_{\text{I}}$ vibrational level are available for excitation because RET couples them to the lower states of the laser transition. Rapid intramodal relaxation implies that each vibrational mode has an individual Boltzmann distribution and therefore a well-defined temperature. Furthermore, energy transfer between the ν_1 mode and the ν_2 mode is fast (hence $T_1 = T_2$) because of the accidental degeneracy between ν_1 and $2\nu_2$. From these observations, we can conclude that T_{tr} , T_{rot} , T_1 , T_2 , and T_3 are all well defined; furthermore, $T_{\text{tr}} = T_{\text{rot}}$ and $T_1 = T_2$. Thus only three independent parameters (T_{tr} , T_1 , T_3) are required to describe the laser-

generated nonequilibrium rovibrational distribution in the CO_2 molecules.

In addition to being a compact descriptor of the vibrational level population distribution, the vibrational temperature is conveniently related to the IR emission rates because of the dependence of emission rates on the vibrational level. Thus vibrational temperatures, in addition to being well defined, are the most compact and useful parameters to describe PLIF signal levels. For each vibrational mode, the emission rate of photons at the fundamental energy $k_B \Theta$ can be related in a straightforward manner to that mode's vibrational temperature T_{vib} . We note that the Einstein A coefficients for fundamental emission from level v to level $v - 1$ in a harmonic oscillator are proportional to v :

$$A_{v \rightarrow v-1} = vA, \quad (12)$$

where $A \equiv A_{1 \rightarrow 0}$ is the rate of emission from $v = 1$ to $v = 0$ ($A \approx 420 \text{ s}^{-1}$ for the ν_3 mode of CO_2). For simplicity, we assume that emission rates are independent of the rotational state. Then, the ensemble-averaged emission rates corresponding to fundamental ($\Delta v = 1$) transitions are given as a sum of the emission rates for each vibrational level, weighted by each level's population fraction N_v/N :

$$A_{\text{avg}} = \sum_v \frac{N_v}{N} A_{v \rightarrow v-1} = \sum_v \frac{N_v}{N} vA. \quad (13)$$

The vibrational energy per molecule e of a harmonic-oscillator vibrational level is also proportional to the quantum number v :

$$e = k_B v \Theta, \quad (14)$$

and similarly the ensemble-averaged energy per molecule e_{vib} in a harmonic-oscillator mode is given by a population-fraction-weighted sum of vibrational level energies:

$$e_{\text{vib}} = \sum_v \frac{N_v}{N} k_B v \Theta. \quad (15)$$

Because Eqs. (13) and (15) have the same functional form, the ensemble-averaged emission rate per molecule corresponding to single-quantum emission can be shown to be proportional to the energy in that vibrational mode:

$$A_{\text{avg}} = A \frac{e_{\text{vib}}}{k_B \Theta}. \quad (16)$$

Equation (16) thus relates the fundamental emission from a vibrational mode to the energy contained within that mode.

Given Eq. (16), the emission rate can be related directly to temperature. The energy of a nondegenerate harmonic-oscillator mode can be written as a function of the mode's vibrational temperature¹⁰:

$$e_{\text{vib}} = \frac{k_B \Theta}{\exp(\Theta/T_{\text{vib}}) - 1}. \quad (17)$$

From Eqs. (16) and (17), the average fundamental emission rate per molecule for a vibrational mode can be described as a simple function of the vibrational temperature T_{vib} :

$$A_{\text{avg}} = A \frac{1}{\exp(\Theta/T_{\text{vib}}) - 1}. \quad (18)$$

Equation (18) can be used to describe the fluorescence yield ψ_{sat} in terms of the laser-induced change in the ν_3 temperature T_3 . Before laser pumping, the system is at equilibrium at temperature T , and the translational, rotational, and vibrational temperatures are equal: $T_{\text{tr}} = T_1 = T_3 \equiv T$. During laser pumping (for which we denote temperatures with an asterisk), the system is driven into a nonequilibrium distribution. Each absorbed 10.6- μm photon removes one molecule from the $10^0_0_1$ level (which has one ν_1 quantum of symmetric stretch energy) and places it in the 00^0_1 level (which has one ν_3 quantum of antisymmetric stretch energy). Thus the laser excitation causes the ν_1 mode to lose energy and the ν_3 mode to gain energy, and during laser excitation $T_1^* < T_{\text{tr}}^* < T_3^*$. The effect of the laser is to generate a nonequilibrium T_3^* with an attendant increase in emission at 4.3 μm .

If the laser-perturbed ν_3 temperature T_3^* is assumed constant throughout the pulse, the fluorescence yield ψ_{sat} can be written simply as the difference between laser-perturbed and ambient emission rates multiplied by the exposure time τ :

$$\psi_{\text{sat}} = (A_{\text{avg},T_3^*} - A_{\text{avg},T})\tau. \quad (19)$$

Thus the fluorescence yield is given by

$$\psi_{\text{sat}} = A\tau \left[\frac{1}{\exp(\Theta_3/T_3^*) - 1} - \frac{1}{\exp(\Theta_3/T) - 1} \right]. \quad (20)$$

Note that the term in brackets is the increase in ν_3 mode energy per molecule caused by laser pumping, normalized by the vibrational energy spacing $k_B\Theta_3$.

Because the pulse energy is high and $k_{\text{laser}} > k_{\text{inter}}$, simple results for the laser-perturbed ν_3 temperature T_3^* can be obtained when we ignore vibration-to-translation and intermodal vibration-to-vibration transfer and assume that the excitation fully saturates the transition. In this case, the laser drives the populations in the $10^0_0_1$ and 00^0_1 levels to be equal. Assuming harmonic oscillators, the vibrational population fractions f of the $10^0_0_1$ and 00^0_1 levels are simple functions of the vibrational temperatures and the total vibrational partition function Q_{vib} (Ref. 10):

$$f_{10^0_0_1} = \frac{\exp(-\Theta_1/T_1^*)}{Q_{\text{vib}}}, \quad (21)$$

$$f_{00^0_1} = \frac{\exp(-\Theta_3/T_3^*)}{Q_{\text{vib}}}. \quad (22)$$

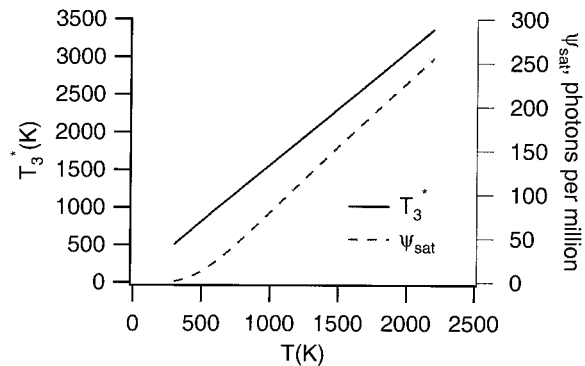


Fig. 3. Predictions of the three-temperature model for the laser-pumped ν_3 mode temperature [T_3^* , (K)] and the fluorescence yield [ψ_{sat} , (photons per million CO_2 molecules)] as a function of initial temperature.

Because the populations in the $10^0_0_1$ and 00^0_1 states are equal during strong laser excitation, from Eqs. (21) and (22) we infer that, under conditions of laser-induced saturation, $\Theta_3/T_3^* = \Theta_1/T_1^*$. With this relation, a straightforward analysis leads to a relation for T_3^* as a function of T (see Appendix A). Results for T and ψ_{sat} are shown in Fig. 3.

The results above are independent of both gas constituents and have a temperature dependence that, although significant because the transition occurs between excited states, is easily calculated *a priori*. Saturation of the absorption transition minimizes laser intensity dependence because stimulated emission competes with stimulated absorption. Collecting laser-prompt fluorescence (i.e., collecting fluorescence only during the laser pulse) minimizes VET rate dependence because the upper vibrational level population during the exposure is controlled by the saturated excitation, and vibrational level dynamics play only a second-order role. Thus ψ_{sat} is essentially unaffected by the efficiency of VET mechanisms that deplete the upper vibrational level. This independence with regard to VET rates is in contrast to ϕ_{lin} , which can be inversely proportional to excited-state deexcitation rates, and makes saturated excitation an attractive way to simplify PLIF signal interpretation.

Detailed VET modeling confirms the quantitative accuracy of the three-temperature model and its simplifying effect on the interpretation of PLIF signal. The detailed VET model discussed in Ref. 3 (approximately 80 vibrational levels and 14,000 energy-transfer processes) has been used with pump-laser source terms to integrate excited-state lifetimes over the camera exposure time and generate predictions for ψ_{sat} as a function of flow parameters. Results for pure CO_2 are shown in Fig. 4, which compares predictions from the simple three-temperature model with results of two detailed calculations. These calculations show that the three-temperature model successfully matches the fluorescence signal predicted by a detailed VET model; the approximations of the three-temperature model (vibrational modes

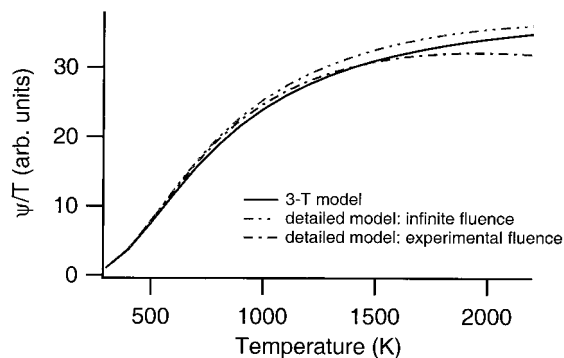


Fig. 4. Comparison of LIF signal levels at a constant CO₂ mole fraction as predicted by the three-temperature (3-T) model and a detailed rate equation model. For the detailed model, results are shown for both 1 J/cm² (corresponding to typical PLIF experiments) and infinite fluences.

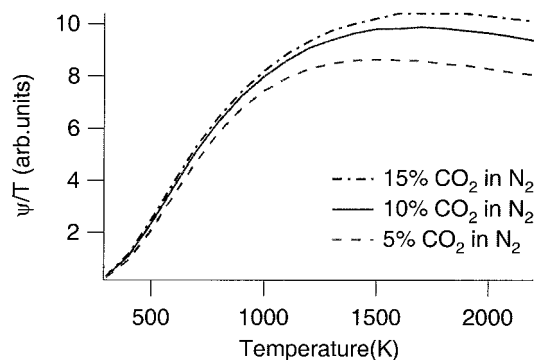
that are independent and harmonic, $T_1 = T_2$, $T_{tr} = T_{rot}$) are thus shown to be accurate.

In addition to confirming the validity of the three-temperature model, the detailed rate equation model predicts the variation of the IR PLIF signal with laser power or changes in the collisional bath. Laser fluences corresponding to those used experimentally (1 J/cm²) generate an IR PLIF signal that is almost completely saturated—within 15% of the signal level for completely saturated (infinite-fluence) excitation. With CO₂ laser pumping, the signal is not strongly affected by changes in laser intensity, CO₂ mole fraction, or H₂O mole fraction that affect VET rates by one or two orders of magnitude.³ Evidence of this is presented in Fig. 5 in which variations of CO₂ and H₂O mole fractions that lead to orders of magnitude difference in VET rates are shown, in the presence of strong excitation, to have only minor ($\pm 15\%$) effects on IR LIF signal levels. Thus saturated excitation techniques can be applied confidently to flows with large variations in CO₂, N₂, or H₂O levels that would render uninterpretable the LIF signal resulting from linear excitation.

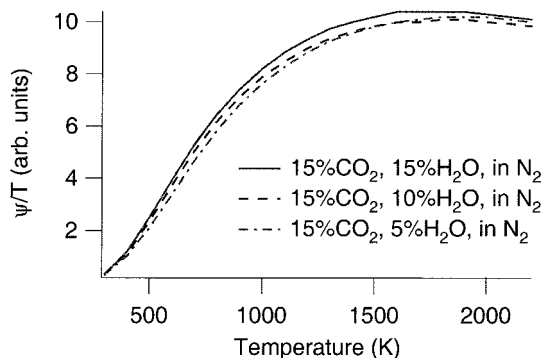
3. Experimental Setup and Techniques

The basic experimental setup shown in Fig. 6 is used to demonstrate the utility of TEA CO₂ laser excitation and confirm the validity of the previous analyses. The CO₂ laser (Lasertechnics Blazer 2000) generates pulses at 10.6 μm with energy up to 5 J. These pulses correspond primarily to the $P(20)$ transition of the $00^0_1 \rightarrow 10^0_1$ emission band at 944.194 cm⁻¹, with small contributions (10%) from the $P(18)$ and $P(22)$ transitions at 945.980 and 942.383 cm⁻¹, respectively. These contributions come early in the pulse before the $P(20)$ line builds up enough intensity to dominate the cavity gain. The pulse length is typical of TEA lasers, with an early 100-ns FWHM peak followed by a slowly decaying (2- μs) tail [see Fig. 9(b) for a graphical representation]. The $P(20)$ line output is gain narrowed to 300 MHz.

Fluorescence was imaged through 4.1–4.5- μm interference filters onto one or two 256 \times 256 InSb



(a)



(b)

Fig. 5. IR LIF signal normalized by CO₂ mole fraction for saturated excitation of CO₂. Effect of (a) CO₂ and (b) H₂O mole fractions.

cameras (Santa Barbara Focalplane SBF 134) with a quantum efficiency of 0.85, a variable exposure time (minimum 300 ns), and a 14-bit dynamic range. Only one camera is required to generate the IR PLIF image; however, in flows with luminous backgrounds, a second camera is triggered before the laser pulse and is used to record and subsequently reject flow luminosity that is present in the absence of laser excitation. Details of dual-image techniques have been described previously.^{2,25} Because the IR PLIF signal in the saturated limit is proportional to the sheet thickness, IR PLIF images of the flow field are also normalized by averaged reference images of a uniform-concentration isothermal flow field. This

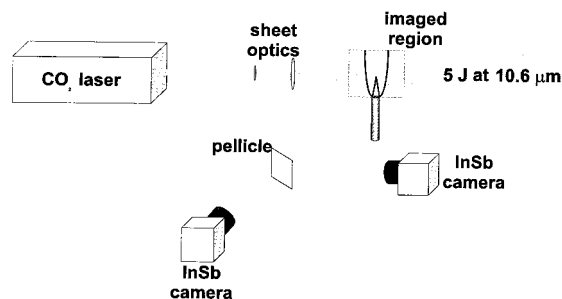


Fig. 6. Experimental setup for saturated IR PLIF measurements.

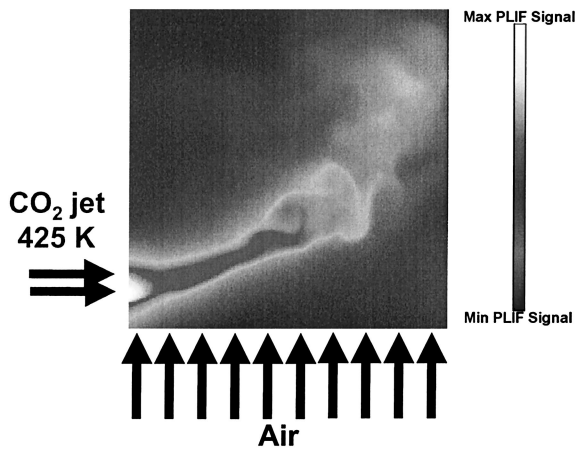


Fig. 7. CO_2 IR PLIF imaging of an unsteady transverse 425 K CO_2 jet in an air coflow.

normalization induces small (5%) errors because of imperfect saturation, particularly in the extreme spatial and temporal regions of the laser sheet where the irradiance approaches zero, but otherwise eliminates spatial signal variations caused by changes in sheet thickness.

4. Results

IR PLIF imaging has been demonstrated in two flows. For imaging experiments, we expanded and formed the CO_2 laser output into a sheet using aluminum-coated or BaF_2 optics. Sheet thickness was $570 \mu\text{m}$ at the focal point with an effective Rayleigh range of 3 cm. Local laser fluence throughout the images varied by a factor of 2 because of laser spatial profile nonuniformity, sheet focusing, and laser attenuation. Spatial resolution perpendicular to the laser sheet is estimated to be $1200 \mu\text{m}$ and is due in part to saturation effects (which give the spatial distribution of the PLIF signal a larger FWHM than the beam-waist FWHM). For the $11 \text{ cm} \times 11 \text{ cm}$ images here, in-plane resolution is limited by optical aberrations and pixel cross talk and is estimated to be $1400 \mu\text{m}$. This resolution, corresponding to a spatial dynamic range of 80, is typical for images collected with our camera systems.

PLIF images are presented for two simple test cases. As a low-temperature demonstration, we imaged an unsteady transverse 425 K CO_2 jet ($d = 7 \text{ mm}$) in an air coflow using a two-camera technique; background luminosity is quite minor ($S/B = 20$) for this flow but was nonetheless removed with the second camera. Exposure times of $2 \mu\text{s}$ were used. The background image was triggered $4 \mu\text{s}$ before the PLIF image, giving an overall temporal resolution of $6 \mu\text{s}$. A sample result is shown in Fig. 7. The peak signal-to-noise ratio for these single-shot images is typically 50, and the minimum detectable concentration at 425 K, 1 atm is $2.7 \times 10^{17} \text{ molecules/cm}^3$ (1000-parts per million mole fraction). Signal in these images is proportional to the CO_2 mole fraction and ψ_{sat}/T .

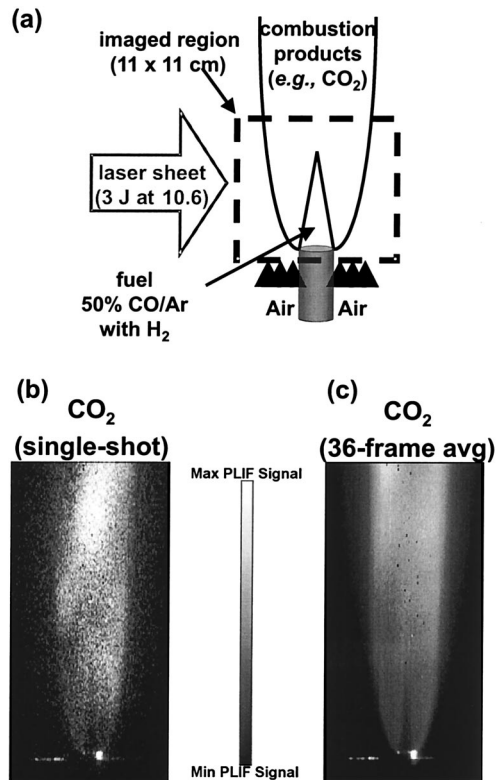


Fig. 8. CO_2 IR PLIF imaging in a CO/H_2 flame. (a) Flame schematic, (b) single-shot image, (c) 36-frame average. Images are cropped horizontally.

In addition to visualization of low-temperature mixing processes, IR PLIF imaging with a CO_2 laser is capable of visualizing high-temperature flows. CO_2 was imaged in a flame fueled primarily by a 50% CO and 50% Ar mixture (2% H_2 added for stability). A single-camera technique was used in this case because the flow was steady and the images at the camera framing rates (in this case 20 Hz) could be reliably subtracted. To minimize flame luminosity, the camera was exposed for the first $1 \mu\text{s}$ of the laser pulse. Results are shown in Fig. 8. The peak signal-to-noise ratio for single-shot images is typically ~ 6 , and the minimum detectable concentration at flame conditions is $1.4 \times 10^{17} \text{ molecules/cm}^3$ (2% CO_2 mole fraction). Again, signal levels in these images are proportional to the CO_2 mole fraction and ψ_{sat}/T . For the temperatures typical of nascent CO_2 as measured in this image, ψ_{sat}/T is roughly independent of temperature.

As indicated above, pumping an excited state leads to a fluorescence signal with appreciable temperature dependence. Although this effect is moderate for images of nascent CO_2 , mixing processes with varying temperatures and cold CO_2 regions motivate the design of excitation schemes with a flat response to temperature. This can be achieved when we combine optical parametric oscillator (OPO) pumping of the $20^0_{11} \leftarrow 00^0_0$ transition at $2.0 \mu\text{m}$ with the CO_2 laser pumping of the $00^0_1 \leftarrow 10^0_1$ transition at $10.6 \mu\text{m}$, as is shown in Fig. 9. Experimental realization

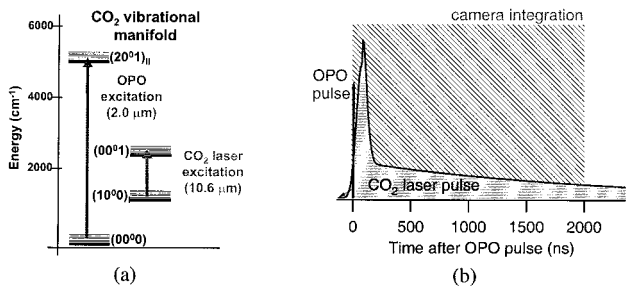


Fig. 9. Combined OPO–CO₂ laser excitation scheme. (a) Excitation steps shown on an energy-level diagram, (b) excitation steps shown on a timing diagram.

of the 2.0- μm pumping scheme is discussed in Ref. 3. The OPO excitation pulse (approximately simultaneous with the start of the CO₂ laser pulse but only 6 ns in length) effectively increases T_1^* ; fast coupling of the $20^0_{1\text{II}}$ and 10^0 states by intramodal energy transfer then leads to an increase in signal. Detailed calculations indicate that experimentally convenient fluences can be chosen such that ψ_{sat}/T is roughly constant with temperature over the range 300–2200 K. We confirmed this by measuring single-point LIF signals at a constant mole fraction (which are proportional to ψ_{sat}/T) as a function of temperature and comparing them with the results of the detailed calculation (Fig. 10). Temperatures up to 900 K were explored. We focused the laser to a 500- μm waist using a 150-mm ZnSe spherical lens, and LIF was measured in the potential core of a heated 10% CO₂/Ar jet. As can be seen in Fig. 10, the experimental data match the predictions well. The effect of the OPO excitation step is clear at low temperatures, for which the Boltzmann fraction of the pumped rovibronic state is large and the 2.0- μm laser pumping is efficient. At higher temperatures, the effect of the OPO step decreases as the Boltzmann

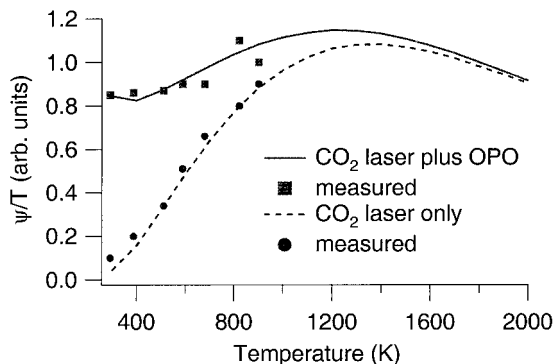


Fig. 10. LIF signal at constant CO₂ mole fraction as a function of temperature for two excitation schemes. Comparison of calculations with measured results. CO₂ laser excitation is employed in the saturated regime. OPO excitation uses fluence of 20 mJ/cm² on the $R(30)$ line of the $20^0_{1\text{II}} \leftarrow 00^0$ transition. CO₂ laser fluence of 10 J/cm² is used, although excitation is insensitive to this value. Experimental results are relative, and a single normalization parameter is used to match both experimental sets to the calculation.

fraction of the pumped rovibronic state decreases; the signal is then dominated by the CO₂ laser pumping. Uniform response with temperature over the wide range shown in Fig. 10 is not achievable by use of linear excitation.³

5. Conclusions

We have presented new IR PLIF imaging techniques for CO₂ that use a high-pulse-energy TEA CO₂ laser to saturate the $P(20)$ absorption transition of the $00^0_{1\text{I}} \leftarrow 10^0_{0\text{I}}$ band at 10.6 μm . An examination of energy-transfer rates has shown that all rotational states of several vibrational levels ($10^0_{0\text{I}}$, $10^0_{0\text{II}}$, and 02^2_0) are pumped indirectly by the TEA laser because its 2- μs pulse length is long enough to allow substantial RET and VET to occur during the laser pulse. This energy redistribution as well as fast intramodal transfer justifies use of a simple three-temperature model to analyze state distributions. When combined with short exposure times provided by our IR cameras, the long, high-energy pulse makes the fluorescence signal easily interpretable in the context of the three-temperature model. Imaging results from a 425 K unsteady transverse CO₂ jet and a laminar coflowing CO/H₂ diffusion flame have been presented, with minimum detectable concentrations of 2.7×10^{17} and 1.4×10^{17} molecules/cm³, respectively. These results demonstrate the ability of simple, inexpensive TEA lasers to generate high IR PLIF signals suitable for single-shot, high-signal-to-noise ratio imaging in a variety of flows.

IR PLIF schemes based on TEA laser excitation alone generate a signal that increases with temperature. Calculations over the 300–2200 K range have been confirmed by single-point LIF measurements over the 300–900 K range and show that the addition of an OPO excitation step at 2.0 μm that pumps the $20^0_{1\text{II}} \leftarrow 00^0$ transition can be implemented to generate a fluorescence yield that is roughly independent of temperature over the 300–2200 K range. This technique can be applied straightforwardly for PLIF imaging.

Appendix A: Calculation of T_3^*

Recall that, before laser excitation, the system is at equilibrium at temperature T , therefore $T = T_{\text{tr}} = T_1 = T_3$. T_{rot} and T_2 need not be specified because $T_{\text{rot}} = T_{\text{tr}}$ and $T_2 = T_1$. During laser excitation, the system is nonequilibrium, so the distribution must be described by three temperatures (T_{tr}^* , T_1^* , T_3^*). From conservation of vibrational energy we have

$$e_{\text{vib}}^* = e_{\text{vib}} + \frac{N_{p,\text{abs}}}{N} k_B(\Theta_3 - \Theta_1), \quad (\text{A1})$$

which states that the difference between the vibrational energies during (e_{vib}^*) and before (e_{vib}) laser pumping is equal to the number of photons absorbed per molecule ($N_{p,\text{abs}}/N$) times the photon energy [$k_B(\Theta_3 - \Theta_1)$]. The number of absorbed photons is

given by the difference between the ν_3 mode energy during and before the laser pulse:

$$\frac{N_{p,abs}}{N} k_B \Theta_3 = \frac{k_B \Theta_3}{\exp(\Theta_3/T_3^*) - 1} - \frac{k_B \Theta_3}{\exp(\Theta_3/T) - 1}. \quad (A2)$$

The vibrational energies for CO₂ can be written as follows (note that ν_2 is doubly degenerate):

$$e_{vib} = \frac{k_B \Theta_1}{\exp(\Theta_1/T_1) - 1} + \frac{2k_B \Theta_2}{\exp(\Theta_2/T_2) - 1} + \frac{k_B \Theta_3}{\exp(\Theta_3/T_3) - 1}, \quad (A3)$$

$$e_{vib}^* = \frac{k_B \Theta_1}{\exp(\Theta_1/T_1^*) - 1} + \frac{2k_B \Theta_2}{\exp(\Theta_2/T_2^*) - 1} + \frac{k_B \Theta_3}{\exp(\Theta_3/T_3^*) - 1}. \quad (A4)$$

Equations (A2)–(A4) can then be substituted into Eq. (A1). Using both $T_1^* = T_2^*$ and $T_3^*/\Theta_3 = T_1^*/\Theta_1$, we obtain

$$\begin{aligned} & \frac{\Theta_1}{\exp(\Theta_1/T) - 1} + \frac{2\Theta_2}{\exp(\Theta_2/T) - 1} + \frac{\Theta_1}{\exp(\Theta_3/T) - 1} \\ &= \frac{\Theta_1}{\exp(\Theta_3/T_3^*) - 1} + \frac{2\Theta_2}{\exp(\Theta_3\Theta_2/\Theta_1 T_3^*) - 1} \\ &+ \frac{\Theta_1}{\exp(\Theta_3/T_3^*) - 1}. \end{aligned} \quad (A5)$$

Equation (A5) can be solved for T_3^* as a function of T , and Eq. (20) can then be used to predict the fluorescence yield.

This research was supported by the U.S. Air Force Office of Scientific Research, Aerospace and Materials Sciences Directorate, with Julian Tishkoff as technical monitor. The authors thank Jay B. Jeffries for insightful comments regarding the manuscript.

References

1. B. J. Kirby and R. K. Hanson, "Planar laser-induced fluorescence imaging of carbon monoxide using vibrational (infrared) transitions," *Appl. Phys. B* **69**, 505–507 (1999).
2. B. J. Kirby and R. K. Hanson, "Imaging of CO and CO₂ using infrared planar laser-induced fluorescence," *Proc. Combust. Inst.* **28**, 253–259 (2000).
3. B. J. Kirby and R. K. Hanson, "Linear excitation schemes for infrared planar laser-induced fluorescence imaging of CO and CO₂," *Appl. Opt.* (2001) (to be published).
4. M. B. Long, D. C. Fourchette, and M. C. Escoda, "Instantaneous Ramanography of a turbulent diffusion flame," *Opt. Lett.* **8**, 244–246 (1983).
5. J. M. Seitzman, J. Haumann, and R. K. Hanson, "Quantitative two-photon LIF imaging of carbon monoxide in combustion gases," *Appl. Opt.* **26**, 2892–2899 (1987).
6. N. Georgiev and M. Aldén, "Two-dimensional imaging of flame species using two-photon laser-induced fluorescence," *Appl. Spectrosc.* **51**, 1229–1237 (1997).
7. G. Juhlin, H. Neij, M. Versluis, B. Johansson, and M. Aldén,

- "Planar laser-induced fluorescence of H₂O to study the influence of residual gases on cycle-to-cycle variations in SI engines," *Combust. Sci. Technol.* **132**, 75–97 (1998).
8. L. S. Rothman and L. D. G. Young, "Infrared energy levels and intensities of carbon dioxide—II," *J. Quant. Spectrosc. Radiat. Transfer* **25**, 505–524 (1981).
9. G. Herzberg, *Molecular Spectra and Molecular Structure II. Infrared and Raman Spectra of Polyatomic Molecules* (Krieger, Malabar, Fla., 1945).
10. W. G. Vincenti and C. H. Kruger, Jr., *Introduction to Physical Gas Dynamics* (Krieger, Malabar, Fla., 1965).
11. F. Rachet, M. Margottin-Maclou, A. Henry, and A. Valentin, "Q-branch line mixing effects in the (20⁰)₁ ← 01¹₀ and (12²)₀ ← 01¹₀ bands of carbon dioxide perturbed by N₂, O₂, and Ar and in the 13¹₀ ← 00⁰₀ and 13¹₀ ← 01¹₀ bands of pure nitrous oxide," *J. Mol. Spectrosc.* **175**, 315–326 (1996).
12. M. Margottin-Maclou, F. Rachet, C. Boulet, A. Henry, and A. Valentin, "Q-branch line mixing effects in the (20⁰)₁ ← 01¹₀ and (12²)₀ ← 01¹₀ bands of carbon dioxide," *J. Mol. Spectrosc.* **172**, 1–15 (1995).
13. R. Rodrigues, Gh. Blanquet, J. Walrand, B. Khalil, R. Le Doucen, F. Thibault, and J.-M. Hartmann, "Line-mixing effects in Q branches of CO₂. I: Influence of parity in Δ ↔ Π bands," *J. Mol. Spectrosc.* **186**, 256–268 (1997).
14. B. Lavorel, G. Millot, R. Saint-Loup, H. Berger, L. Bonamy, J. Bonamy, and D. Robert, "Study of collisional effects on band shapes of the $\nu_1/2\nu_2$ Fermi dyad in CO₂ gas with stimulated Raman spectroscopy. I. Rotational and vibrational relaxation in the $2\nu_2$ band," *J. Chem. Phys.* **93**, 2176–2184 (1990).
15. L. L. Strow and B. M. Gentry, "Rotational collisional narrowing in an infrared CO₂ Q-branch studied with a tunable diode laser," *J. Chem. Phys.* **84**, 1149–1156 (1986).
16. M. Margottin-Maclou, A. Henry, and A. Valentin, "Line mixing in the Q-branches of the $\nu_1 + \nu_2$ band of nitrous oxide and of the (11¹)₀ ← (02²)₀ band of carbon dioxide," *J. Chem. Phys.* **96**, 1715–1723 (1992).
17. T. Huet, N. Lacombe, and A. Lévy, "Line mixing effects in the Q branch of the 10⁰ ← 01¹₀ transition of CO₂," *J. Mol. Spectrosc.* **138**, 141–161 (1989).
18. R. Berman, P. Duggan, P. M. Sinclair, A. D. May, and J. R. Drummond, "Direct measurements of line-mixing coefficients in the $\nu_1 + \nu_2$ Q branch of CO₂," *J. Mol. Spectrosc.* **182**, 350–363 (1997).
19. J.-M. Hartmann and C. Boulet, "Line mixing and finite duration of collision effects in pure CO₂ infrared spectra: fitting and scaling analysis," *J. Chem. Phys.* **94**, 6406–6419 (1991).
20. C. P. Rinsland and L. L. Strow, "Line mixing effects in solar occultation spectra of the lower stratosphere: measurements and comparisons with calculations for the 1932-cm⁻¹ CO₂ Q branch," *Appl. Opt.* **28**, 457–464 (1989).
21. B. Gentry and L. L. Strow, "Line mixing in a N₂-broadened CO₂ Q branch observed with a tunable diode laser," *J. Chem. Phys.* **86**, 5722–5730 (1987).
22. G. Millot and C. Roche, "State-to-state vibrational and rotational energy transfer in CO₂ gas from time-resolved Raman-infrared double-resonance experiments," *J. Raman Spectrosc.* **29**, 313–320 (1998).
23. G. D. Billing, "Semiclassical calculation of energy transfer in polyatomic molecules. VII. Intra- and inter-molecular energy transfer in N₂ + CO₂," *Chem. Phys.* **67**, 35–47 (1982).
24. G. D. Billing, "Semiclassical calculation of energy transfer in polyatomic molecules. XI. Cross sections and rate constants for Ar + CO₂," *Chem. Phys.* **91**, 327–339 (1984).
25. B. K. McMillin, J. L. Palmer, and R. K. Hanson, "Temporally resolved, two-line fluorescence imaging of NO temperature in a transverse jet in a supersonic cross flow," *Appl. Opt.* **32**, 7532–7545 (1993).